ADVANCED FUNCTIONAL MATERIALS
www.afm-journal.de

Photothermal Killing of Cancer Cells by the Controlled Plasmonic Coupling of Silica-Coated Au/Fe_2O_3 Nanoaggregates

*Georgios A. Sotiriou, Fabian Starsich, Athanasia Dasargyri, Moritz C. Wurnig, Frank Krumeich, Andreas Boss, Jean-Christophe Leroux, and Sotiris E. Pratsinis**

Tumor ablation by thermal energy via the irradiation of plasmonic nanoparticles is a relatively new oncology treatment. Hybrid plasmonic-superparamagnetic nanoaggregates (50–100 nm in diameter) consisting of SiO_2-coated Fe_2O_3 and Au (≈30 nm) nanoparticles were fabricated using scalable flame aerosol technology. By finely tuning the Au interparticle distance using the SiO_2 film thickness (or content), the plasmonic coupling of Au nanoparticles can be finely controlled bringing their optical absorption to the near-IR that is most important for human tissue transmittance. The SiO_2 shell facilitates also dispersion and prevents the reshaping or coalescence of Au particles during laser irradiation, thereby allowing their use in multiple treatments. These nanoaggregates have magnetic resonance imaging (MRI) capability as shown by measuring their r2 relaxivity while their effectiveness as photothermal agents is demonstrated by killing human breast cancer cells with a short, four minute near-IR laser irradiation (785 nm) at low flux (4.9 W cm^{-2}).

1. Introduction

Plasmonic materials such as Au and Ag show great potential for use in energy,[1] catalysis,[2] optoelectronics,[3] and biomedical applications, to name a few.[4] When these metals are brought to the nanoscale, they exhibit a drastic increase in light absorption.[5] This effect originates from the interaction of the nanoparticles with electromagnetic radiation, which gives rise to collective oscillations of the metal surface electrons. These oscillations depend on the wavelength of the incident light and reach a maximum when the electrons are in their resonance state: the so-called localized surface plasmon resonance frequency.[5] Part of the oscillation energy is converted into heat via relaxation processes.[6] These processes depend on various factors, such as the particle size and shape, the aggregation state, the surrounding dielectric medium and the properties of the particle surfaces.[7,8]

The potential of this efficient conversion of light into heat has been investigated for the treatment of cancer by in-vivo photothermal tumor ablation.[9] When such nanoparticles are irradiated at an appropriate wavelength, they convert light into heat and kill the cancer cells. This phenomenon has been demonstrated with spherical gold nanoparticles of approximately 40 nm in diameter that were selectively taken up by epithelial carcinoma cells.[10] Upon laser irradiation at 514 nm, which is close to the plasmon resonance frequency of these Au nanoparticles at 530 nm, the cells were killed. Furthermore, gold nanoparticles can also be employed for drug delivery from temperature-responsive polymers upon laser irradiation.[11]

Human tissue, however, exhibits a high transmittance of electromagnetic irradiation in the near-IR region (i.e., wavelengths between 700 and 900 nm).[12] Therefore, such a process would be more efficient if the plasmonic particles absorbed light in this spectral region. One way to shift the absorption of plasmonic particles to higher wavelengths is to change their shape. For example, gold nanoshells[9] and nanorods[13] exhibit high light absorption in the near-IR region. As such, they have shown promising results for the photothermal ablation of cancer cells, both in-vitro[13,14] and in-vivo.[9,15] The fabrication of such nanoparticles, however, involves a multistep, tedious and expensive process, and its limited scalability and reproducibility hinder the commercialization of such nanoparticles.[16] Furthermore, gold nanoshells are rather large (>120 nm), which might hinder their biodistribution, and their absorption cross section is lower than that of solid gold nanoparticles,

Dr. G. A. Sotiriou, F. Starsich, Dr. F. Krumeich, Prof. S. E. Pratsinis
Particle Technology Laboratory
Institute of Process Engineering
Department of Mechanical and Process Engineering, ETH Zurich
Sonneggstrasse 3, CH-8092 Zurich, Switzerland
E-mail: sotiris.pratsinis@ptl.mavt.ethz.ch
Dr. G. A. Sotiriou
Department of Environmental Health
Harvard University
665 Huntington Ave., Boston 02115, MA, USA
A. Dasargyri, Prof. J.-C. Leroux
Drug Formulation & Delivery
Institute of Pharmaceutical Sciences
Department of Chemistry and Applied Biosciences, ETH Zurich
Wolfgang-Pauli-Strasse 10, CH-8093 Zurich, Switzerland
Dr. M. C. Wurnig, Dr. A. Boss
Institute of Diagnostic and Interventional Radiology
University Hospital Zurich
Raemistrasse 100, CH-8091 Zurich, Switzerland

DOI: 10.1002/adfm.201303416

thus requiring a higher laser power to kill cancer cells.[10] In contrast, gold nanorods may show strong absorption in their longitudinal mode in the near-IR spectral region; this behavior, however, depends on their spatial orientation.[17] Furthermore, the rods may melt and reshape into spheres during laser irradiation,[18] which would decrease their near-IR absorption and may inhibit subsequent in-vivo therapeutic sessions.

Another way to influence the light absorption (and color) of plasmonic materials is to tune their spatial configuration.[19] As two or more plasmonic particles are brought closer together, the field enhancement between them increases (hot spots).[20] This plasmonic coupling gives rise to specific interparticle interactions[21] that can broaden their optical absorption.[22] This effect can be exploited in broadband energy applications[23] or surface-enhanced Raman scattering.[24]

An ideal bionanoprobe for theranostics should exhibit multiple functionalities.[25] In particular, superparamagnetism is an attractive characteristic, as it facilitates placement and manipulation of the probe.[26] Hybrid, multifunctional plasmonic-magnetic nanoparticles[27] offer several advantages, including multiple imaging techniques such as magnetic resonance imaging (MRI).[28,29] Superparamagnetic nanoparticles can also be guided by an external magnetic field[26] to enhance the specific targeting of tumors in combination with antibody-mediated receptor binding.[30] An additional mode of therapeutic action can be exploited by magnetic hyperthermia, in which the temperature rises due to rapid switching of the external magnetic field.[31] Additionally, such nanoparticles can be coated with amorphous SiO_2 that offers facile surface functionalization.[32] Such a hermetic coating can also reduce any toxicity of the core nanoparticle[33] and make it hydrophilic and easy to functionalize with (bio)molecules.[34]

Here, we create novel hybrid multifunctional plasmonic bionanoprobes that are suitable for photothermal tumor ablation using a single-step, fast and high-purity gas-phase process with high reproducibility and proven scalability.[35] Aggregates (<100 nm in diameter) consisting of multiple gold and iron-oxide nanoparticles are coated in situ during their synthesis with an amorphous and nanothin silica shell of closely controlled thickness. This allows for fine tuning of their optical absorption in the near-IR region, thereby facilitating the nanoparticles' use in photothermal tumor treatment.

2. Results and Discussion

2.1. Morphology

Figure 1a shows a high-resolution transmission electron microscopy (TEM) image of Au/Fe_2O_3 nanoparticles coated with 2.6-nm amorphous SiO_2 shells.[27] The darker spherical particles correspond to Au, while the Fe_2O_3 particles appear gray. The energy-dispersive X-ray (EDX) spectrum of the nanoparticles (Figure 1b) confirms the elemental composition (Au, Fe, Si, and O). The Cu signal originates from the copper grid that was used during the electron microscopy analysis. Beyond this, no other elements are detected, indicating that the nanoparticles are impurity-free. From the high-resolution TEM results (Figure 1a), it is possible to distinguish the amorphous SiO_2 shell from the crystalline Au and Fe_2O_3, in which some crystal planes are detectable.

An aberration-corrected scanning transmission electron microscope (STEM) was employed to obtain detailed images of these nanoparticles. Figure 1 shows the same area of these SiO_2-coated Au/Fe_2O_3 nanoparticles imaged with Z-contrast using a high-angle annular dark field (HAADF) detector (c), a phase-contrast detector (d) and a secondary electron detector (e). In Figure 1c, the bright spheres correspond to the Au nanoparticles because they have the highest atomic number (Z) of all elements present. The faint gray areas in the Z-contrast image indicate the presence of less heavy scatterers (e.g., the dotted circles in Figure 1c), which are inferred to be Fe_2O_3 and SiO_2. The crystalline Fe_2O_3 is also detectable as areas that exhibit lattice fringes in the phase-contrast STEM images (the dotted circles in Figure 1d). In this image, the contrast is inverted, as in a conventional HRTEM image, showing the Au particles with a darker color. The surface of the entire nanoaggregate is visible in the secondary electron image, revealing the ball-like morphology of the aggregates of silica-coated Au and Fe_2O_3 nanoparticles (Figure 1e).

Figure 1 also shows a HAADF-STEM (Z-contrast) image (f) and the corresponding elemental mappings obtained by EDX spectroscopy for Au (g), Fe (h), Si (i) and all three elements together in a merged image (j). The Si map (Figure 1i) contains the most noise because of the relatively small amount of SiO_2 (5.7 wt%). Comparison between the Au and Fe maps (Figures 1g,h) clearly reveals that these elements are separated, as previously shown in Figure 1a. The Au and Fe_2O_3 nanoparticles are located predominantly next to each other, forming Janus- or dumbbell-like nanoaggregates, as in the case of Ag/Fe_2O_3.[27] By comparing the Si map (Figure 1i) and the merged image (Figure 1j), it can be seen that the SiO_2 encapsulates both the Au and Fe_2O_3 nanoparticles.[36] This result is confirmed by ζ-potential measurements, which show a complete SiO_2 coating for the Au/Fe_2O_3, with theoretical thicknesses of > 1.4 nm (Figure S1, Supporting Information).[37]

The SiO_2 shell is formed in situ in the gas phase by swirl injection of the Si precursor vapor following the formation of the core nanoparticle (here Au/Fe_2O_3).[32] In this way, the presence of the SiO_2 does not influence the inherent properties of the core materials, as in the cases of pure TiO_2,[32] Ag[33] and Fe_2O_3.[38] This lack of influence due to SiO_2 is verified here by monitoring the magnetic properties of the Au/Fe_2O_3 nanoparticles.

2.2. Superparamagnetism

Figure 2 shows the magnetic hysteresis for SiO_2 shells of theoretical thicknesses ranging from 0 to 5.9 nm. The maximum magnetization for all samples is in agreement with that of flame-made ≈20 nm γ-Fe_2O_3.[38] Furthermore, all samples exhibit near-superparamagnetic behavior, as there is minimal coercivity.[38] In fact, the bare Au/Fe_2O_3 nanoparticles (orange line) exhibit the largest coercivity of ≈50 T (Figure 2, inset diagram). As the SiO_2 shell thickness increases, the coercivity progressively decreases to ≈20 T for a 5.9-nm-thick shell (red line). This reduction could be attributed to the minimization of Fe_2O_3 magnetic interactions for the thicker SiO_2 shells, causing the sample to become more superparamagnetic.[38]

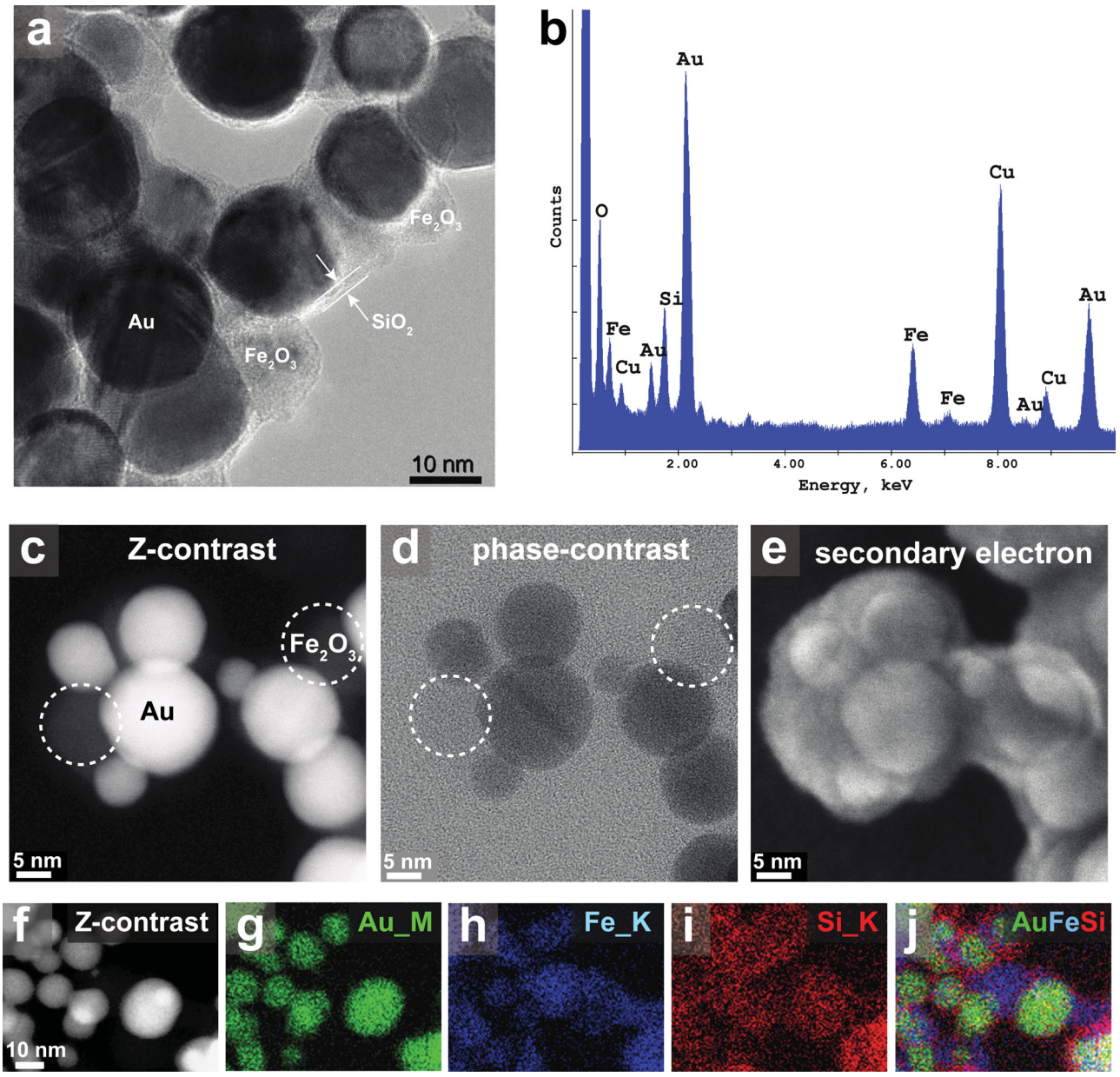

Figure 1. a) High-resolution TEM image of Au/Fe_2O_3 nanoparticles coated with 2.6-nm-thick amorphous SiO_2 shells (5.7 wt% SiO_2). b) EDX spectrum of the same sample, verifying its elemental composition. STEM images of a nanoaggregate of SiO_2-coated Au/Fe_2O_3 nanoparticles recorded with different detectors: c) HAADF (Z-contrast), d) bright-field (phase-contrast), and e) secondary electron. f) HAADF-STEM Z-contrast image and the corresponding elemental EDXS mappings for g) Au, h) Fe, i) Si, and j) all three elements together in a merged image.

Furthermore, the Fe_2O_3 component of these hybrid plasmonic-superparamagnetic nanoaggregates (Figure 1e) allows for their external magnetic manipulation and placement. The inset image of Figure 2 shows aqueous suspensions of bare Au/Fe_2O_3 (0 nm SiO_2 shell) nanoparticles in the absence ($B = 0$) and presence ($B > 0$) of a magnetic field. Upon the application of this field, all the nanoparticles (highlighted by the dotted ellipse) are attracted to the side of the cuvette that is adjacent to the magnet, making the suspension transparent.[27] This finding further verifies the formation of hybrid nanoaggregates (Au/Fe_2O_3) and the absence of any "free" Au nanoparticles, which would remain after the application of the magnetic field, as has been shown for similar Ag/Fe_2O_3 nanosuspensions.[27]

Figure 2b shows the relaxation rate R2 (calculated from the T2 transverse relaxation time) of the hybrid Au/Fe_2O_3 nanoaggregates with a 1.4-nm-thick SiO_2 shell dispersed in agar gel as a function of the Fe_2O_3 concentration. The relaxation rate R2 increases linearly for higher Fe_2O_3 concentrations, as expected. From this graph, the relaxivity rate r2, which is an indicator of the MRI-agent performance, can be calculated. The observed value of r2 = 325 mM^{-1} s^{-1} at 4.7 T is comparable to that of other hybrid Janus-like (121 mM^{-1} s^{-1} at 3 T)[39] and core-shell

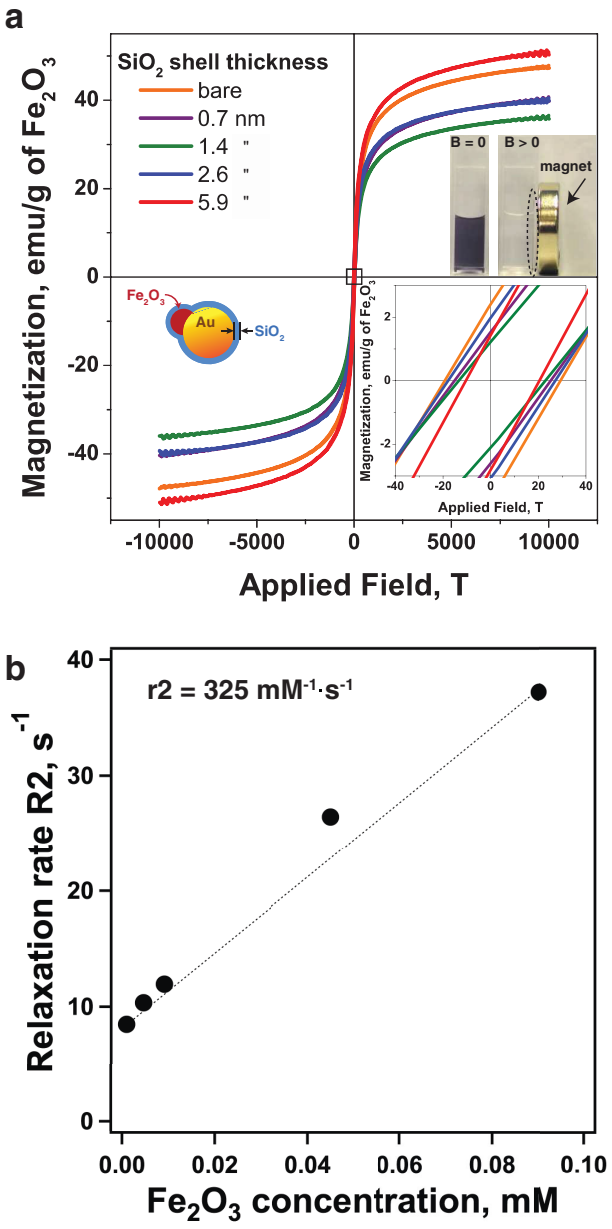

Figure 2. a) Magnetic hysteresis curves for Au/Fe_2O_3 nanoparticles with different SiO_2 shell thicknesses. The inset diagram shows a magnification of the region of the graph at low magnetic fields, which highlights the coercivity and remanence of the particles, thereby establishing their near-superparamagnetic behavior. The inset image shows aqueous suspensions of bare (0-nm SiO_2 shell thickness) Au/Fe_2O_3 nanoparticles before ($B = 0$) and after ($B > 0$) the application of an external magnetic field, which clears the suspension and proves that all the Au nanoparticles are attached to superparamagnetic Fe_2O_3 nanoparticles. b) The relaxation rate R2 of Au/Fe_2O_3 nanoparticles coated with 1.4-nm-thick SiO_2 shells in agar gel as a function of the Fe_2O_3 concentration. The relaxivity r2 is also shown.

gold/iron-oxide nanoparticles (390 mM^{-1} s^{-1} at 9.4 T)[40] and that of commercial inorganic MRI agents (59–358 mM^{-1} s^{-1}).[41] The nanothin hydrophilic SiO_2 shell surrounding the core Au/Fe_2O_3 nanoparticles facilitates the interaction between the contrast agent and the neighboring water protons, resulting in MRI contrast enhancement and allowing these nanoparticles to be employed as MRI agents.[41]

The average Au crystal size of these hybrid nanoaggregates is ≈30 nm, as verified by X-ray diffraction (Figure S2, Supporting Information). It should be noted that Fe_2O_3 is present in its crystalline form, as verified by the electron microscopy analysis (Figure 1), but the characteristic γ-Fe_2O_3 diffraction peaks are too weak to be detected in the presence of Au (Figure S2, Supporting Information) because of the low Fe_2O_3 content (12.9–14.8 wt% depending on the SiO_2 content). The hydrophilic SiO_2 shell facilitates nanoaggregate dispersion and, at the same time, prevents the formation of micron-sized flocs.[33] The average hydrodynamic size of these SiO_2-coated nanoaggregates when dispersed in deionized water and phosphate-buffered saline solution is about 50–100 nm (Figure S1, Supporting Information), which is within the desired range for efficient biodistribution upon their employment as therapeutic agents.[40,42] Therefore, each nanoaggregate consists of stochastically distributed multiple Au and Fe_2O_3 nanoparticles, while the encapsulating SiO_2 shell acts as a dielectric spacer.[43] At the closest possible proximity of two Au nanoparticles, their interparticle distance x is twice the thickness of the SiO_2 shell (inset in **Figure 3**a). Therefore, as the SiO_2 shell thickness increases, the Au interparticle distance x also increases.

2.3. Plasmonic Properties and Photothermal Effect

The interparticle distance of plasmonic particles strongly affects their optical properties.[19] Figure 3a shows the optical absorption spectra of aqueous suspensions of the Au/Fe_2O_3 nanoparticles (each containing an identical Au concentration of 10 mg L^{-1}) for varying interparticle distance x (and different SiO_2 shell thicknesses). The characteristic Au plasmon absorption band near 550 nm is present (red dotted line) for all samples. The absorption in the 530- to 550-nm range is typical for Au nanospheres of approximately 40 nm in diameter[10,44] and is attributed to the dipole-type electron resonance.[8] However, as the Au nanospheres come closer to each other with decreasing interparticle distance x, the induced plasmonic coupling[22] broadens the optical absorption up to ~800 nm (purple dotted line at 785 nm). Furthermore, the plasmonic peak becomes sharper and stronger for the largest $x = 11.8$ nm. This result indicates that for $x > 10$ nm, there is little, if any, interparticle interaction or plasmonic coupling, in agreement with the literature.[22] The inset of Figure 3a shows the aqueous suspensions of these samples. The color ranges from dark gray ($x = 0$) to bright purple ($x = 11.8$ nm), consistent with the corresponding absorption spectra presented in this figure.

In fact, if the absolute absorption intensities at 550 (triangles) and 785 nm (circles) are plotted as a function of interparticle distance x (Figure 3b; the SiO_2 content in units of wt% is also shown on the top axis), the intensity at 550 nm decreases for smaller x, in agreement with the literature.[8] With increasing plasmonic coupling (decreasing x), the main peak attributed to the dipole resonances becomes weaker. In contrast, the absolute intensity in the biomedically important near-IR region (700–800 nm) increases with

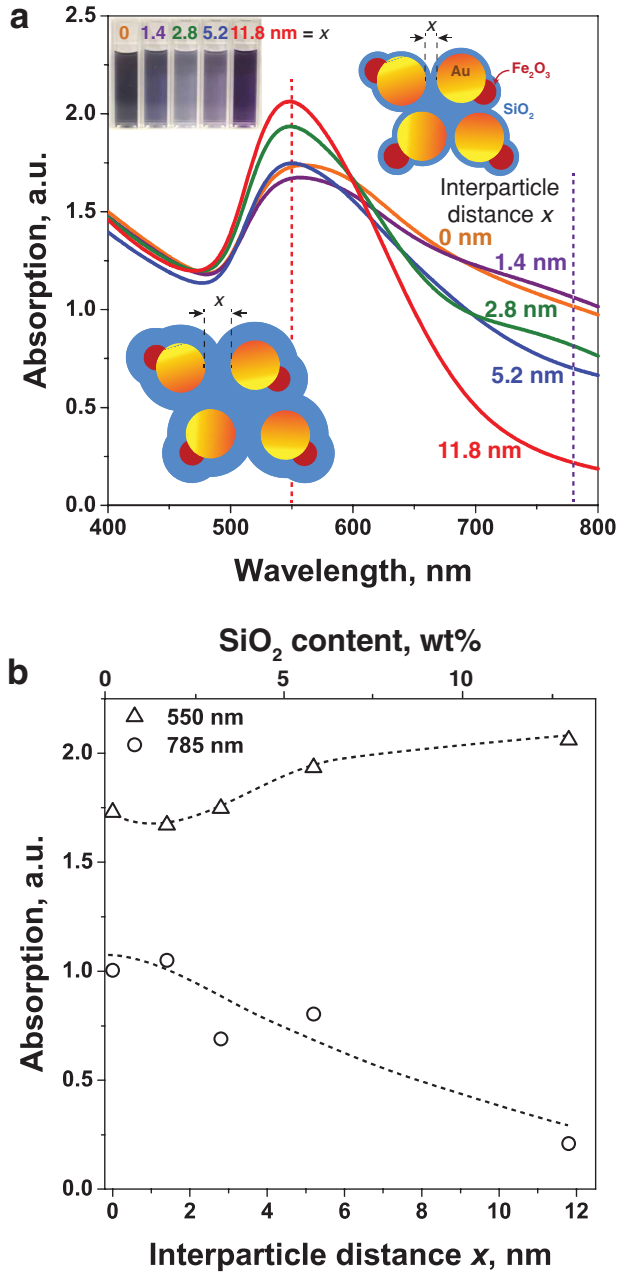

Figure 3. a) Optical absorption spectra of SiO_2-coated Au/Fe_2O_3 nanoaggregates for various average interparticle distances x (twice the SiO_2 shell thickness). An interparticle plasmonic coupling occurs that broadens the spectra, which becomes stronger as x decreases. b) Absolute absorption intensities at 550 (triangles) and 785 nm (circles) as a function of the interparticle distance x (or the SiO_2 content, which is shown in units of wt% on the top axis). The spectra at 550 nm demonstrate that for thicker coatings, the Au nanoaggregates behave like single, non-interacting Au nanospheres. The spectra at 785 nm indicate that thinly coated Au nanoparticles in a highly aggregated state are most attractive for the photothermal treatment of cancer cells.

increasing plasmonic coupling. The absorption intensity provides a good estimate of the photothermal efficiency upon irradiation at these wavelengths, especially for nanospheres smaller than 40 nm, which have high absorption coefficients and minimal scattering.[44] Gold nanorods also have high absorption coefficients, while nanoshells exhibit high scattering coefficients.[45]

Indeed, upon the near-IR (785 nm) laser irradiation of these hybrid Au/Fe_2O_3 nanoaggregates immobilized in agar gel (Au concentration of 30 mg L^{-1}), there is a gradual temperature increase, ΔT (**Figure 4**a, inset). The final ΔT depends on the applied laser radiation flux (power per unit area, blue and red lines). For example, the sample with an interparticle distance of x = 1.4 nm reached ΔT_{max} = 30 °C at the highest laser radiation flux of 4.9 W cm^{-2}, with a plateau after 180 s (Figure 4a). After the irradiation stops, the temperature rapidly decreases to the initial conditions.

When the ΔT_{max} values of the SiO_2-coated Au/Fe_2O_3 nanoaggregates are plotted as a function of the interparticle distance x (Figure 4b), it can be seen that the highest ΔT_{max} values are obtained at the lowest x. In fact, as expected, the observed trend is identical to that of the absolute absorption intensities at 785 nm (Figure 3b, circles, and Figure S3, Supporting Information). This further corroborates that these Au nanospheres exhibit high absorption cross sections and cause minimal light scattering,[10] and therefore, they efficiently convert the laser light into heat.

We also examined the photothermal performance of state-of-the-art gold nanoshells (≈150 nm in diameter) and gold nanorods (10 nm × 40 nm) immobilized in agar for identical Au concentrations (30 mg L^{-1}) and laser-irradiation conditions (4.9 W cm^{-2}), following literature protocols.[46] The nanoshells reached a comparable ΔT_{max} = 38.8 °C, while the nanorods exhibited the highest ΔT_{max} of 71 °C. Furthermore, we explored the thermal stability of the hybrid nanoaggregates and compared it to that of the nanoshells and nanorods. Figure 4c shows the optical absorption spectra of nanoaggregates (x = 2.8 nm, green line), nanoshells (red line) and nanorods (blue line) deposited on glass slides (72 μg of Au) before (solid line) and after (broken line) near-IR (785 nm) laser exposure (15 W cm^{-2}) for 30 min.

After laser irradiation, the absorption spectrum of the nanoaggregates (broken green line) remains rather stable and quite high in the near-IR region. In contrast, the absorption spectra of both the nanoshells (red broken line) and the nanorods (blue broken line) drastically decrease after the laser irradiation due to particle melting and reshaping. More specifically, the longitudinal mode (the peak at 808 nm) of the nanorod absorption (blue line) completely disappears. This indicates that the nanorods have been reshaped and formed into spheres, as is further indicated by the increase in the 525-nm peak (Figure 4c). Similarly, the near-IR absorption of the nanoshells drastically decreases, indicating their reshaping. In contrast, the thermally stable SiO_2 shell inhibits Au particle growth and reshaping. Although the photothermal efficiency of the hybrid nanoaggregates is lower than that of the nanorods and nanoshells, the nanoaggregates maintain their near-IR absorption, which should facilitate their employment in multiple thermal treatments.

2.4. Cell Uptake and Photothermal Treatment

The uptake of plasmonic nanoparticles by cells can be verified by hyperspectral microscopy.[47] Hybrid Au/Fe_2O_3

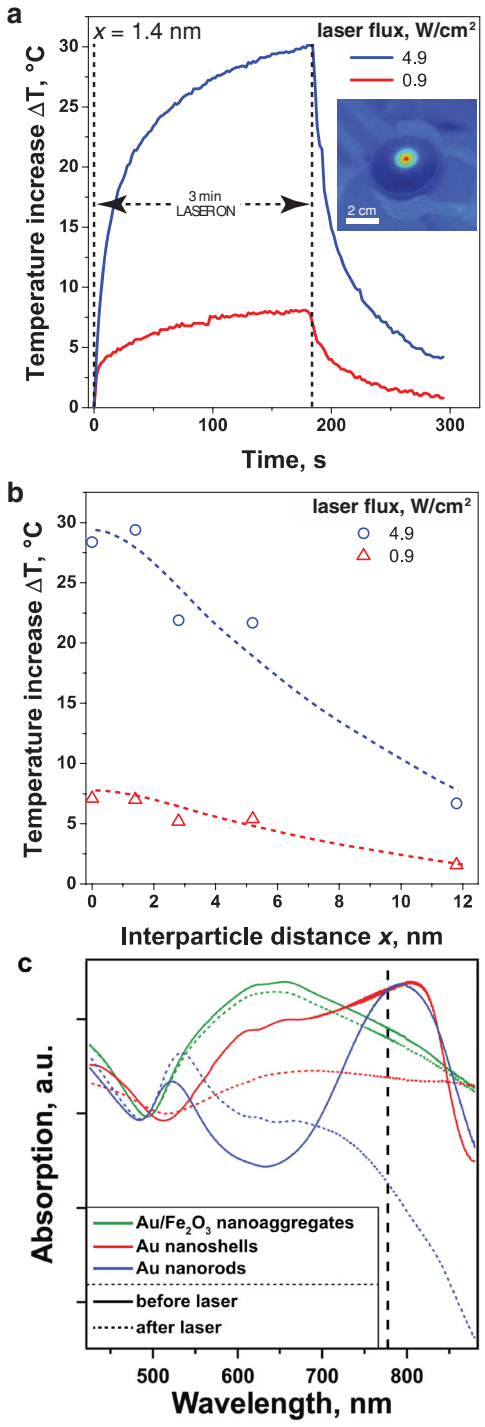

Figure 4. a) Evolution of the temperature difference, ΔT, of agar gel containing aggregates of Au/Fe_2O_3 nanoparticles (30 mg L^{-1} of Au) with an average interparticle distance of $x = 1.4$ nm upon subjection to a near-IR laser irradiation flux of 4.9 W cm^{-2}. When the laser is turned on, the agar temperature increases, as detected by an infrared camera (inset). b) The maximum temperature increase, ΔT, of the above agar gel after 3 min of laser irradiation as a function of the interparticle distance x. The photothermal effect is stronger for smaller x. c) The optical absorption spectra of Au/Fe_2O_3 nanoaggregates ($x = 2.8$ nm, green lines), nanoshells (red lines) and nanorods (blue lines) deposited on glass slides before (solid lines) and after (broken lines) laser irradiation (15 W cm^{-2} for 30 min).

nanoparticles (interparticle distance $x = 2.8$ nm) were incubated with human breast cancer cells (MDA-MB-231) at Au concentrations of 0–20 mg L^{-1}. **Figure 5** shows dark-field microscopy images of pure cells (a) and cells incubated with 10 (b) and 20 mg L^{-1} (c) of Au nanoparticles, along with corresponding hyperspectral images (d–f) after the application of a spectral classification algorithm for each case (see Figure S4 for the nanoparticle spectral library). The presence of Au nanoparticles is detected in the cells as bright spots in the hyperspectral images for both Au concentrations (Figure 5e,f), confirming the nanoparticle uptake. In contrast, the hyperspectral image of the control cells alone (d) does not show the Au nanoparticle signal.

As a proof of concept for the feasibility of using these flame-made plasmonic nanostructures as photothermal tumor-ablation agents, the above nanoparticle-cell cultures were irradiated using a near-IR laser (785 nm, spot size of 5 mm) at 4.9 W cm^{-2} for 4 min. The cell viability was evaluated using a fluorescent assay that labels live cells in green and dead cells in red. **Figure 6** shows the resultant fluorescent microscopy images of glass slides with cells alone (a), cells incubated with particles (20 mg L^{-2} of Au) without any laser irradiation (b), cells alone irradiated with the laser (c) and cells incubated with particles and irradiated with the laser (d). The temperature of each glass slide after 4 min of laser irradiation is also displayed in Figure 6.

The cell viability is not influenced by the mere presence of the particles (Figure 6b) for concentrations up to 50 mg L^{-1} (not shown), as expected, because none of the employed materials exhibits strong toxicity. Furthermore, laser irradiation of the glass slides with the cells alone (without any particles) does not induce any significant temperature increase or cell damage (green cells, Figure 6c). Only in the presence of particles are the human breast cancer cells killed by the laser (red cells, Figure 6d), in which case the slide temperature is increased to 71.8 °C.

Such selective photothermal cancer cell destruction is consistent with those of gold nanoshells (140 nm in diameter) and a 820-nm laser at 80 W cm^{-2},[14] nanospheres (30 nm in diameter)[45] and nanorods (≈10 nm × 40 nm)[13] with an 800-nm laser at 10–20 W cm^{-2}, gold nanoshells (45 nm in diameter) with magnetic iron-oxide cores upon irradiation with a 700-nm pulsed laser[48] and gold nanorods (≈20 nm × 90 nm) attached to iron-oxide nanoparticles (15 nm) with a 785-nm laser[49] at 4.5 W cm^{-2}. However, here, for the first time, cancer cells are killed photothermally using hybrid SiO_2-coated Au/Fe_2O_3 nanoaggregates by exploiting their controlled plasmonic coupling, which also have the potential to be magnetically manipulated and detected.

3. Conclusions

Biocompatible, hybrid, nanothinly SiO_2-coated nanoaggregates (<100 nm) of multiple Au and Fe_2O_3 nanoparticles that are suitable for the in-vivo photothermal ablation of tumors via near-IR laser irradiation were prepared using a scalable gas-phase process. The interparticle distance among the Au nanoparticles is finely tuned by closely controlling the SiO_2 shell thickness

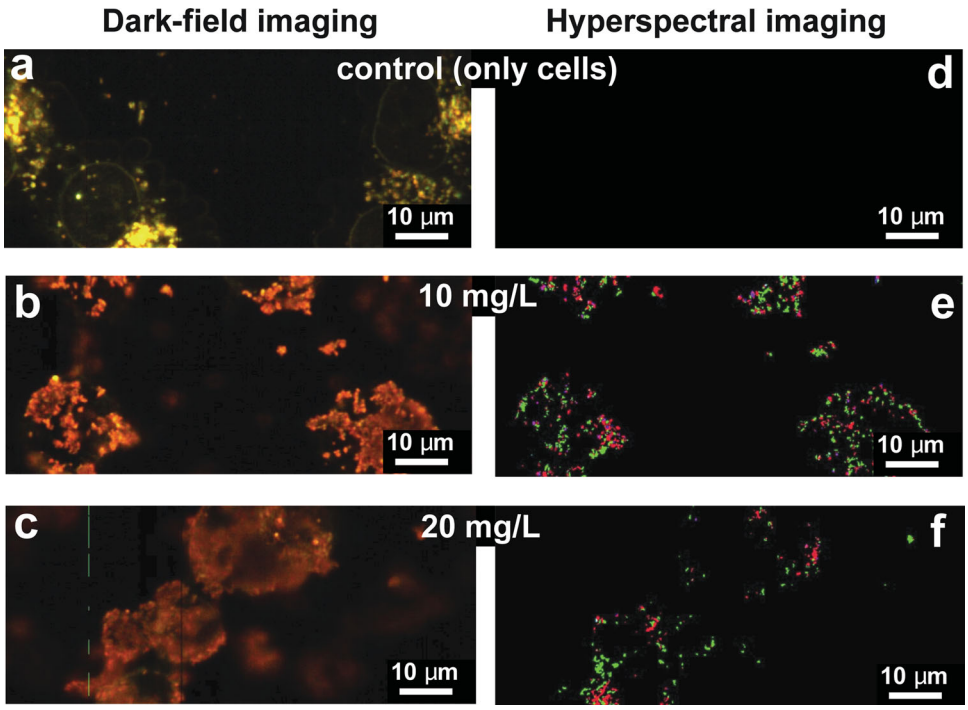

Figure 5. a–c) Dark-field and d–f) hyperspectral images of human breast cancer cells, a,d) alone and incubated with b,e) 10 and c,f) 20 mg L^{-1} Au/Fe_2O_3 nanoparticles. The hyperspectral images verify the presence of Au nanoparticles (bright spots in (e,f)) in the cell cultures. In the absence of any nanoparticles, there is no signal in the hyperspectral image (d).

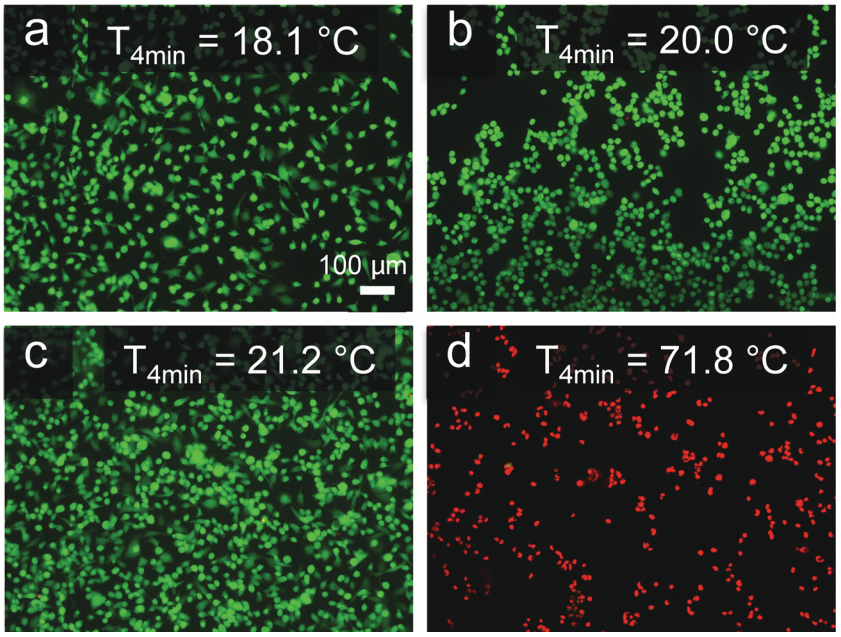

Figure 6. Fluorescent images of breast cancer cells on glass slides stained with LIVE/DEAD dye (green = live, red = dead). a) Cells alone, b) cells incubated with 20 mg L^{-1} Au/Fe_2O_3 nanoparticles without any laser irradiation, c) cells alone irradiated with a laser, and d) cells incubated with particles (20 mg L^{-1}) and irradiated with a laser. The irradiation was applied at a flux (power per area) of 4.9 W cm^{-1} for 4 min. The increase in temperature ΔT_{max} of the glass slides after 4 min of laser irradiation is also shown. Only in the presence of particles are the cells killed by the laser. The scale bars are identical in all images.

to give rise to plasmonic interparticle coupling. This interaction broadens the absorption of these plasmonic nanoparticles to the near-IR spectral region. Therefore, when subjected to near-IR laser irradiation, these hybrid bionanoprobes exhibit a photothermal effect similar to that of state-of-the-art gold nanoshells and nanorods but with superior thermal stability and resistance to reshaping (through melting), which allows for their use in multiple treatments. The feasibility of using such multifunctional plasmonic nanoparticles for photothermal tumor ablation is demonstrated in-vitro with human breast cancer cells.

For successful in-vivo tumor ablation, a tissue temperature of at least 48–50 °C must be achieved.[50] However, the sensitivity of different tissues to heat exposure varies.[51] Therefore, a systematic investigation on the pharmacokinetics of such hybrid nanoparticles must be conducted to ensure maximum accumulation to the tumor site in-vivo. The delivery of such agents to the tumor site can be achieved by passive and active targeting; therefore, surface biofunctionalization is necessary to ensure long circulation times and to bypass the reticuloendothelial system.

The presence of SiO_2 facilitates this biofunctionalization step because its surface chemistry is well understood.

The presence of the hydrophilic SiO_2 shell also promotes the facile dispersion of such nanoparticles in aqueous solutions and biologically relevant media. Furthermore, the SiO_2 shell does not influence the Fe_2O_3 superparamagnetic properties, which offer additional functionality to the bionanoprobe, while the MRI capability of such hybrid nanoparticles is demonstrated by the r2 relaxivity, thereby verifying that the particles can be detected in-vivo.

4. Experimental Section

Multifunctional Au/Fe_2O_3 Nanoparticles with SiO_2 Coating: Multifunctional bare and SiO_2-coated Au/Fe_2O_3 nanoparticles were produced via enclosed flame spray pyrolysis. This dry and scalable synthesis method has been described in detail elsewhere.[32] In brief, a liquid precursor solution was fed at 5 mL min^{-1} into the reactor via a capillary. The solution was then dispersed and sheathed with O_2 gas (5 L min^{-1} and 40 L min^{-1}, respectively; Pan Gas, purity >99%) and ignited by a premixed CH_4/O_2 flame (1.5/3.2 L min^{-1}). The flame was enclosed by a 30-cm quartz glass tube (ID = 45 mm). The SiO_2 coating was applied by swirl injection of N_2 carrying hexamethyldisiloxane (HMDSO) vapor (total flow rate 16 L min^{-1}, Sigma-Aldrich, purity ≥ 99%) through a ring with 16 equidistant openings that was placed on top of the quartz tube. The HMDSO was fed through a bubbler operating at 10 °C. On top of this ring, another 25-cm quartz glass tube was placed. The freshly formed particles were collected on a glass fiber filter with the aid of a vacuum pump. The entire reactor was preheated for 3 min prior to the nanoparticle synthesis using a particle-free solvent (e.g., xylene). The SiO_2 content for the coating was adjusted to values of 0, 1.5, 2.9, 5.7, 9.1, and 13 wt% (SiO_2 wt% = m_{SiO2}/ (m_{Au}+ $m_{Fe_2O_3}$+ m_{SiO_2})) by varying the nitrogen flow through the bubbler (under HMDSO saturation conditions).[32]

Liquid Precursor Solution: The Au precursor (gold III acetate, Alfa Aesar, purity ≥ 99%) was kept at a constant concentration of C_{Au} = 0.25 M. The Fe precursor (iron (III) acetylacetonate, Sigma-Aldrich, purity ≥ 97%) atomic content was also kept constant at 30 at% Fe (at% Fe = mol Fe/(mol Fe + mol Au)) of the core particles. Acetonitrile and 2-ethylhexanoic acid (both Sigma-Aldrich, purity > 97%) were used as solvents at a volume ratio of 1:1. During preparation, the Au and Fe precursors were first separately dissolved in 15 mL of the above solvents. The Fe-containing solution was maintained under constant magnetic stirring, whereas the Au-containing solution was heated in an oil bath at 100 °C for 30 min followed by 10 min of cooling. Thereafter, the two solutions were slowly mixed together under constant stirring and were then immediately sprayed through the FSP unit to avoid any sedimentation. Gold nanoshells (120-nm silica core, 15-nm gold shell, PEG-coated) and gold nanorods (10 nm × 40 nm, CTAB-coated) were purchased from Nanocomposix and Sigma-Aldrich, respectively.

Particle Characterization: Crystal sizes were measured by X-ray diffraction (XRD; Bruker AXS D8 Advanced spectrometer, Cu Kα, 40 kV, 40 mA) and processed using the TOPAS 4 software by fitting the main diffraction peaks to standards. The specific surface area (SSA) was determined by the Brunauer-Emmett-Teller (BET) method (Micrometrics Tristar 3000) at 77 K with N_2, after 1 h of degassing at 150 °C.

Optical absorption measurements were performed via UV/Vis spectroscopy (Cary Varian 500) in aqueous solutions at a concentration of 100 mg/L Au. The samples were analyzed after ultrasonication (Sonics Vibra Cell, 8 kJ, power 70%, pulse on/off 1 s/1 s). Hydrodynamic sizes were obtained by dynamic light scattering (DLS, Zetasizer, Malvern Instruments). The particles were diluted in water at 10 mg L^{-1} and ultrasonicated (Sonics Vibra Cell, 8 kJ, power 70%, pulse on/off 1 s/1 s). The same DLS device was used for ζ-potential measurements by varying the pH through titration (Multi Purpose Titrator – 2, Malvern Instruments) from 4 to 9 with a step size of 1. Particle images were obtained by high-resolution transmission electron microscopy (HRTEM) on a Tecnai F30 microscope (FEI; FEG cathode, at 300 kV, point resolution approx. 2 Å). Scanning transmission electron microscopy (STEM) studies were performed using an aberration-corrected, dedicated STEM (Hitachi HD-2700CS) apparatus equipped with a probe corrector (CEOS). STEM was performed at an acceleration potential of 200 kV (electron gun: cold-field emitter) in the ultra-high resolution mode of this microscope.[52,53] Various detectors can be chosen for imaging in bright-field (BF) and dark-field modes (HAADF). The collection angle in BF mode is selected in such a way that the direct beam and the diffracted beams interfere with one another, generating an interference pattern (phase contrast).[54] A secondary electron detector and an EDX spectrometer (Gemini system, EDAX) were mounted in the electron column above the sample. Magnetic measurements were collected on a Princeton Measurements Corporation vibrating sample magnetometer (VSM).

Relaxivity Measurements: To assess the magnetic characteristics of the nanoparticles with respect to their potential use as MRI contrast agents, their *r2* relaxivity (relaxation of transverse magnetization, "spin-spin interaction") was measured. The decay of the transverse relaxation can be characterized by the transverse relaxation time *T2*, which is the time at which the transverse magnetization has decayed to 37% (e^{-1}) of its initial value after spin excitation. The relaxation rate *R2* is defined as the inverse of the relaxation time ($R2 = 1/T2$). Increasing the concentration of the contrast agent decreases the *T2* relaxation time, as described by the following equation:

$$\frac{1}{T2'} = \frac{1}{T2} + r2 * c \quad (1)$$

where *T2* refers to the intrinsic *T2* time of the tissue/sample, *T2'* is the reduced *T2* time resulting from the contrast agent, *r2* is the transverse relaxivity of the contrast agent, and *c* is the concentration of the contrast-agent. Thus, the relaxivity *r2* of a contrast agent is defined as the potential of the contrast agent to reduce the T2 time, depending on its concentration.

The relaxation times *T2* of different concentrations of nanoparticles (0.001–0.1 mg mL^{-1}, 0.0009–0.09 mM Fe_2O_3) diluted in agar gel were quantified with a 2D fast spin-echo sequence with multiple echoes (TE 11/33/55/77/99 ms; TR 4500 ms; echo train length, 2; FOV 2 cm × 2 cm; matrix 128 × 128; slice thickness 1.5 mm) on a 4.7-T small-animal MRI (PharmaScan 47/16 US; Bruker, Ettlingen, Germany) with a linearly polarized whole-body mouse coil at room temperature. The samples were prepared by first diluting 0.0375 g of agar (Sigma-Aldrich) in 2.5 mL of H_2O followed by heating at 100 °C for 15 min. Thereafter, 2.5 mL of the freshly sonicated aqueous particle suspension was added and briefly mixed. The *T2* relaxation time was calculated from the signal intensities by applying custom-written MATLAB computer scripts. A linear least-squares fit to the equation

$$S(TE) = S(0) * e^{-\frac{TE}{T^2}} + n \quad (2)$$

was performed using an algorithm based on the interior-reflective Newton method. *S*(0) denotes the signal intensity at zero echo-time and *n* denotes the thermal noise. The fitting variables of the algorithm were S(0) and *T2*. The noise term *n* was not fitted but estimated from the mean signal intensity in a ROI selected in the image background outside the object, which appeared to result in better stability of the fit parameters. The relaxivity r2 was calculated as the slope of the linear fit of the inverse *T2* relaxation times obtained for the different concentrations of nanoparticles and MRI contrast agent using Equation 1.

Laser-Heating Experiments: To investigate the heat ablation properties of the produced multifunctional plasmonic particles, a near-IR laser (IRM785TA-3000FC, SLOC Lasers) with a wavelength of 785 nm and absolute powers of 0.18 W and 0.96 W was used as a light source. The temperature was measured by an IR thermal camera (Fluke, Ti110) every

2 s, and final temperatures were obtained after 180 s of heating. The samples were prepared in agar gel, as described above for the relaxivity measurements. The complete (5 mL) resulting agar-gel/nanoparticle mixture was dispersed on Petri dishes (d = 50 mm) to form layers of ≈2 mm in thickness. UV/Vis spectroscopy data (Cary Varian 500) of the cooled, solid, gel-like samples were obtained.

The thermal stability was evaluated by monitoring the optical absorption of nanoaggregates, nanoshells and nanorods deposited on glass slides for identical Au mass (72 μg) and laser irradiation conditions (15 W cm^{-2} for 30 min). For this purpose, 2.4 mL of a 30 mg/L aqueous solution of each sample was deposited on a glass slide, which was then placed on a mildly heated hot plate (80 °C) for 2 h to allow for water evaporation. The absorption of the slides was measured before and after laser treatment.

Cell Culture: MDA-MB-231 cells (ATCC, cell line of metastatic adenocarcinoma of the breast) were cultured in Dulbecco's Modified Eagle Medium (DMEM, Invitrogen) supplemented with 10% fetal bovine serum (FBS, Invitrogen) containing 1% penicillin-streptomycin solution (Invitrogen) in a humidified atmosphere containing 5% CO_2. The cells were grown on round glass cover slips (18 mm in diameter) in 12-well tissue culture plates (TPP) at a concentration of 150 000 cells $well^{-1}$ in 1 mL DMEM and were allowed to grow for 24 h.

Hyperspectral Microscopy: The nanoparticle cell uptake was assessed via hyperspectral microscopy. This imaging system is based on the characteristic scattering profile of gold nanoparticles. Confluent MDA-MB-231 cells on cover slips were incubated with nanoparticles at different concentrations (10, 20, and 50 μg mL^{-1}) in 1 mL HBSS. After 2 h, the nanoparticles were removed, and the cells were washed three times with HBSS before cover slips were placed on the glass slides and sealed with clear nail polish. The slides were imaged using the Cytoviva Hyperspectral Imaging System (Cytoviva Inc.). This system consists of an Olympus BX53 dark-field microscope equipped with a high-resolution Cytoviva 150 adapter, a motorized stage, a visible/near-infrared hyperspectral camera system and a 150-W halogen light source. The diffraction spectrum of the sample at visible and near-IR wavelengths (400–1000 nm) was recorded at each pixel in the images, thereby allowing for a subsequent analysis of the scattered light at any location within the sample. Ten dark-current images were collected at the beginning of each hyperspectral image acquisition and were subtracted from the hyperspectral image data. A spectral classification algorithm (Spectral Angle Mapper) that uses an n-dimensional angle (equal to the number of wavelengths analyzed) was applied to match the pixels on the hyperspectral image to reference libraries that were acquired by analyzing gold nanoparticle samples dispersed in water. The data were obtained and analyzed using ENVI 4.4 software.

Photothermal Therapy: The confluent cells on the cover slips were incubated with different concentrations of nanoparticles (10, 20, and 50 μg mL^{-1}) in 1 mL HBSS for 2 h. The cell monolayers were washed three times with HBSS and irradiated with a near-IR laser (785 nm, 4.9 W cm^{-2}, spot size 5 mm). The cells were then incubated with 200 μL of fresh LIVE/DEAD reagent solution (LIVE/DEAD Viability/Cytotoxicity Kit, Molecular Probes) for 30 min in the dark. The cover slips were mounted on glass microscope slides, sealed with clear nail polish and imaged using an Axioskop 2 MOT Plus microscope equipped with 5/0.16 Plan-Apochromat, 10/0.45 Plan-Apochromat and 20/0.50 Plan-Neofluar objectives and an AxioCam MRc color camera (Carl Zeiss). The images were acquired using AxioVision 4.8 software.

Supporting Information

Supporting Information is available from the Wiley Online Library or from the author. It includes the XRD analysis of the as-prepared nanoparticles, their dynamic light scattering and ζ-potential measurements and results, the correlation between the absolute absorption intensity and the maximum achieved temperature difference of the agar/nanoparticle gels and a dark-field image of the Au/$Fe2O_3$ nanoparticles dispersed in water, along with their scattering profiles.

Acknowledgments

This research was supported by the Swiss National Science Foundation (grant no. 200020–126694) and the European Research Council under the European Union's Seventh Framework Program (FP7/2007–2013, ERC grant agreement no. 247283). The electron microscopy work was performed at the Electron Microscopy Center of the ETH Zurich (EMEZ). G.A.S. was supported by a Swiss National Science Foundation Advanced Researcher fellowship (grant no. 145392).

Received: October 3, 2013
Revised: November 19, 2013
Published online: January 13, 2014

[1] P. Nagpal, N. C. Lindquist, S. H. Oh, D. J. Norris, *Science* **2009**, *325*, 594–597.
[2] N. Liu, M. L. Tang, M. Hentschel, H. Giessen, A. P. Alivisatos, *Nat. Mater.* **2011**, *10*, 631–636.
[3] S. Kawata, A. Ono, P. Verma, *Nat. Photonics* **2008**, *2*, 438–442.
[4] J. N. Anker, W. P. Hall, O. Lyandres, N. C. Shah, J. Zhao, R. P. Van Duyne, *Nat. Mater.* **2008**, *7*, 442–453.
[5] K. A. Willets, R. P. Van Duyne, *Annu. Rev. Phys. Chem.* **2007**, *58*, 267–297.
[6] P. K. Jain, X. H. Huang, I. H. El-Sayed, M. A. El-Sayed, *Acc. Chem. Res.* **2008**, *41*, 1578–1586.
[7] K. L. Kelly, E. Coronado, L. L. Zhao, G. C. Schatz, *J. Phys. Chem. B* **2003**, *107*, 668–677.
[8] D. D. Evanoff, G. Chumanov, *ChemPhysChem* **2005**, *6*, 1221–1231.
[9] L. R. Hirsch, R. J. Stafford, J. A. Bankson, S. R. Sershen, B. Rivera, R. E. Price, J. D. Hazle, N. J. Halas, J. L. West, *Proc. Natl. Acad. Sci. U. S. A.* **2003**, *100*, 13549–13554.
[10] I. H. El-Sayed, X. H. Huang, M. A. El-Sayed, *Cancer Lett.* **2006**, *239*, 129–135.
[11] B. Radt, T. A. Smith, F. Caruso, *Adv. Mater.* **2004**, *16*, 2184–2189.
[12] R. Weissleder, *Nat. Biotechnol.* **2001**, *19*, 316–317.
[13] X. H. Huang, I. H. El-Sayed, W. Qian, M. A. El-Sayed, *J. Am. Chem. Soc.* **2006**, *128*, 2115–2120.
[14] C. Loo, A. Lowery, N. Halas, J. West, R. Drezek, *Nano Lett.* **2005**, *5*, 709–711.
[15] E. B. Dickerson, E. C. Dreaden, X. H. Huang, I. H. El-Sayed, H. H. Chu, S. Pushpanketh, J. F. McDonald, M. A. El-Sayed, *Cancer Lett.* **2008**, *269*, 57–66.
[16] P. Rodgers, *Nat. Nanotechnol.* **2011**, *6*, 607–608.
[17] H. Ma, P. M. Bendix, L. B. Oddershede, *Nano Lett.* **2012**, *12*, 3954–3960.
[18] S. Link, M. A. El-Sayed, *J. Chem. Phys.* **2001**, *114*, 2362–2368.
[19] U. Kreibig, L. Genzel, *Surf. Sci.* **1985**, *156*, 678–700.
[20] W.-S. Chang, B. A. Willingham, L. S. Slaughter, B. P. Khanal, L. Vigderman, E. R. Zubarev, S. Link, *Proc. Natl. Acad. Sci. U. S. A.* **2011**, *108*, 19879–19884.
[21] S. Link, M. A. El-Sayed, *Int. Rev. Phys. Chem.* **2000**, *19*, 409–453.
[22] S. K. Ghosh, T. Pal, *Chem. Rev.* **2007**, *107*, 4797–4862.
[23] X. Dang, J. Qi, M. T. Klug, P.-Y. Chen, D. S. Yun, N. X. Fang, P. T. Hammond, A. M. Belcher, *Nano Lett.* **2013**, *13*, 637–642.
[24] J. A. Creighton, C. G. Blatchford, M. G. Albrecht, *J. Chem. Soc. Faraday Trans.* **1979**, *75*, 790–798.
[25] G. A. Sotiriou, *WIREs Nanomed. Nanobiotechnol.* **2013**, *5*, 19–30.
[26] A. K. Gupta, M. Gupta, *Biomaterials* **2005**, *26*, 3995–4021.
[27] G. A. Sotiriou, A. M. Hirt, P. Y. Lozach, A. Teleki, F. Krumeich, S. E. Pratsinis, *Chem. Mater.* **2011**, *23*, 1985–1992.

[28] R. Weissleder, G. Elizondo, J. Wittenberg, C. A. Rabito, H. H. Bengele, L. Josephson, *Radiology* **1990**, *175*, 489–493.
[29] J. Rahmer, A. Antonelli, C. Sfara, B. Tiemann, B. Gleich, M. Magnani, J. Weizenecker, J. Borgert, *Phys. Med. Biol.* **2013**, *58*, 3965–3977.
[30] C. H. J. Choi, C. A. Alabi, P. Webster, M. E. Davis, *Proc. Natl. Acad. Sci. U. S. A.* **2010**, *107*, 1235–1240.
[31] M. Creixell, A. C. Bohórquez, M. Torres-Lugo, C. Rinaldi, *ACS Nano* **2011**, *5*, 7124–7129.
[32] A. Teleki, M. C. Heine, F. Krumeich, M. K. Akhtar, S. E. Pratsinis, *Langmuir* **2008**, *24*, 12553–12558.
[33] G. A. Sotiriou, T. Sannomiya, A. Teleki, F. Krumeich, J. Vörös, S. E. Pratsinis, *Adv. Funct. Mater.* **2010**, *20*, 4250–4257.
[34] A. Vargas, I. Shnitko, A. Teleki, S. Weyeneth, S. E. Pratsinis, A. Baiker, *Appl. Surf. Sci.* **2011**, *257*, 2861–2869.
[35] S. E. Pratsinis, *AIChE J.* **2010**, *56*, 3028–3035.
[36] A. Teleki, S. E. Pratsinis, K. Wegner, R. Jossen, F. Krumeich, *J. Mater. Res.* **2005**, *20*, 1336–1347.
[37] A. Teleki, M. K. Akhtar, S. E. Pratsinis, *J. Mater. Chem.* **2008**, *18*, 3547–3555.
[38] A. Teleki, M. Suter, P. R. Kidambi, O. Ergeneman, F. Krumeich, B. J. Nelson, S. E. Pratsinis, *Chem. Mater.* **2009**, *21*, 2094–2100.
[39] C. Xu, J. Xie, D. Ho, C. Wang, N. Kohler, E. G. Walsh, J. R. Morgan, Y. E. Chin, S. Sun, *Angew. Chem. Int. Ed.* **2008**, *47*, 173–176.
[40] R. Bardhan, W. Chen, M. Bartels, C. Perez-Torres, M. F. Botero, R. W. McAninch, A. Contreras, R. Schiff, R. G. Pautler, N. J. Halas, A. Joshi, *Nano Lett.* **2010**, *10*, 4920–4928.
[41] H. B. Na, I. C. Song, T. Hyeon, *Adv. Mater.* **2009**, *21*, 2133–2148.
[42] M. E. Davis, Z. Chen, D. M. Shin, *Nat. Rev. Drug Discovery* **2008**, *7*, 771–782.
[43] J. A. Fan, C. Wu, K. Bao, J. Bao, R. Bardhan, N. J. Halas, V. N. Manoharan, P. Nordlander, G. Shvets, F. Capasso, *Science* **2010**, *328*, 1135–1138.
[44] P. K. Jain, K. S. Lee, I. H. El-Sayed, M. A. El-Sayed, *J. Phys. Chem. B* **2006**, *110*, 7238–7248.
[45] X. Huang, W. Qian, I. H. El-Sayed, M. A. El-Sayed, *Lasers Surg. Med.* **2007**, *39*, 747–753.
[46] A. M. Elliott, R. J. Stafford, J. Schwartz, J. Wang, A. M. Shetty, C. Bourgoyne, P. O'Neal, J. D. Hazle, *Med. Phys.* **2007**, *34*, 3102–3108.
[47] A. Pratsinis, P. Hervella, J.-C. Leroux, S. E. Pratsinis, G. A. Sotiriou, *Small* **2013**, *9*, 2576–2584.
[48] T. A. Larson, J. Bankson, J. Aaron, K. Sokolov, *Nanotechnology* **2007**, *18*, 325101.
[49] C. G. Wang, J. Chen, T. Talavage, J. Irudayaraj, *Angew. Chem. Int. Ed.* **2009**, *48*, 2759–2763.
[50] W. C. Dewey, *Int. J. Hyperthermia* **2009**, *25*, 3–20.
[51] S. Sapareto, W. Dewey, *Int. J. Radiat. Oncol. Biol.* **1984**, *10*, 787–800.
[52] H. Inada, L. Wu, J. Wall, D. Su, Y. Zhu, *J. Electron. Microsc.* **2009**, *58*, 111–122.
[53] F. Krumeich, E. Mueller, R. A. Wepf, R. Nesper, *J. Phys. Chem. C* **2011**, *115*, 1080–1083.
[54] F. Krumeich, E. Mueller, R. A. Wepf, *Micron* **2013**, *49*, 1–14.